UC San Diego

UC San Diego Previously Published Works

Title

Understanding LOC/SOC phenomenology in tokamaks

Permalink

https://escholarship.org/uc/item/8pb0r9wq

Journal

Nuclear Fusion, 60(10)

ISSN

0029-5515

Authors

Rice, JE
Citrin, J
Cao, NM
et al.

Publication Date

2020-10-01

DOI

10.1088/1741-4326/abac4b

Copyright Information

This work is made available under the terms of a Creative Commons Attribution-NonCommercial-NoDerivatives License, availalbe at https://creativecommons.org/licenses/by-nc-nd/4.0/

Peer reviewed

eScholarship.org Powered by the California Digital Library
University of California

Published as:
Nucl. Fusion **60** (2020) 105001
https://doi.org/10.1088/1741-4326/abac4b

ACCEPTED MANUSCRIPT

Understanding LOC/SOC phenomenology in tokamaks

To cite this article before publication: John E Rice *et al* 2020 *Nucl. Fusion* in press https://doi.org/10.1088/1741-4326/abac4b

Manuscript version: Accepted Manuscript

Accepted Manuscript is "the version of the article accepted for publication including all changes made as a result of the peer review process, and which may also include the addition to the article by IOP Publishing of a header, an article ID, a cover sheet and/or an 'Accepted Manuscript' watermark, but excluding any other editing, typesetting or other changes made by IOP Publishing and/or its licensors"

This Accepted Manuscript is **© 2020 IAEA, Vienna**.

During the embargo period (the 12 month period from the publication of the Version of Record of this article), the Accepted Manuscript is fully protected by copyright and cannot be reused or reposted elsewhere.
As the Version of Record of this article is going to be / has been published on a subscription basis, this Accepted Manuscript is available for reuse under a CC BY-NC-ND 3.0 licence after the 12 month embargo period.

After the embargo period, everyone is permitted to use copy and redistribute this article for non-commercial purposes only, provided that they adhere to all the terms of the licence https://creativecommons.org/licences/by-nc-nd/3.0

Although reasonable endeavours have been taken to obtain all necessary permissions from third parties to include their copyrighted content within this article, their full citation and copyright line may not be present in this Accepted Manuscript version. Before using any content from this article, please refer to the Version of Record on IOPscience once published for full citation and copyright details, as permissions will likely be required. All third party content is fully copyright protected, unless specifically stated otherwise in the figure caption in the Version of Record.

View the article online for updates and enhancements.

This content was downloaded from IP address 137.110.34.16 on 20/08/2020 at 17:02

Understanding LOC/SOC Phenomenology in Tokamaks

J.E. Rice[‡], J. Citrin[†], N.M. Cao[‡], P.H. Diamond[♯], M. Greenwald[‡] and B.A. Grierson[♮]

[‡]*PSFC, MIT, Cambridge, Massachusetts 02139, USA*

[†]*DIFFER, De Zaale 20, 5612 AJ Eindhoven, The Netherlands*

[♯]*UCSD, La Jolla, California 92093, USA*

[♮]*PPPL, Princeton, New Jersey 08543, USA*

Abstract

Phenomenology of Ohmic energy confinement saturation in tokamaks is reviewed. Characteristics of the linear Ohmic confinement (LOC) and saturated Ohmic confinement (SOC) regimes are documented and transformations in all transport channels across the LOC/SOC transition are described, including rotation reversals, "non-local" cut-off and density peaking, in addition to dramatic changes in fluctuation intensity. Unification of results from nearly 20 devices indicates that the LOC/SOC transition occurs at a critical value of the product of the density, edge safety factor and device major radius, and that this product increases with toroidal magnetic field. Comparison with gyro-kinetic simulations suggests that the effects of sub-dominant TEMs are important in the LOC regime while ITG mode turbulence dominates with SOC.

Accepted Manuscript

1. Introduction

Following the confirmation of high temperature operation in the T-3 device in 1969 [1], there was an explosion in construction of tokamaks worldwide, and subsequently in the 1970s there were numerous studies of energy confinement in purely Ohmically heated plasmas. Exploring a range of densities made available through gas puffing, it was soon discovered that, remarkably, the global energy confinement time increases linearly with increasing electron density: the linear Ohmic confinement (LOC) regime [2, 3, 4, 5, 6, 7, 8, 9, 10, 11, 12, 13, 14, 15, 16, 17, 18, 19]. Also notable is that this so-called Alcator scaling is a ubiquitous observation on all tokamaks. Comparison of results from a large number of devices indicated a dependence of the slope on machine dimensions and edge safety factor. The future looked rosy as it appeared that the $n\tau T$ fusion triple product would potentially increase quadratically with density. By the 80s this optimism subsided when it was found that the energy confinement time saturates [7, 9, 13, 14, 17, 20, 21, 22, 23, 24] above a critical density. This saturated Ohmic confinement (SOC) regime is also remarkably ubiquitous in tokamak operation [25, 26, 27, 28, 29, 30, 31, 32, 33, 34, 35, 36, 37, 38, 39, 40, 41, 42, 43, 44, 45, 46, 47]. An early example of both regimes is shown in Fig.1 from the Alcator C device for 8 T deuterium discharges with edge safety factor q_{cyl} between 3.5 and 4.8 [9, 13]. As

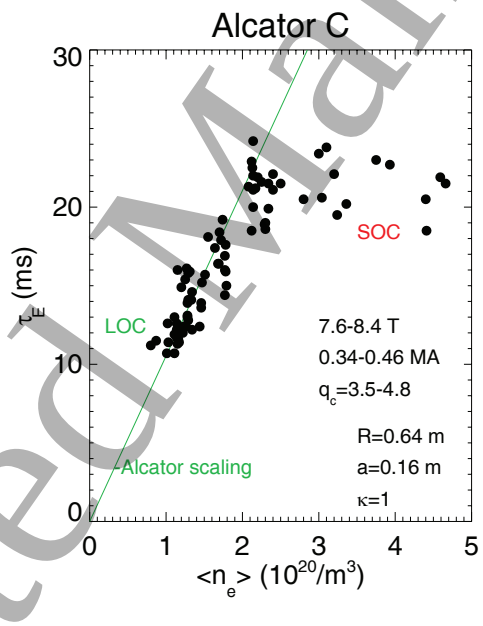

Figure 1: The global energy confinement time as a function of average density for circular Alcator C discharges with $B_T \sim 8$ T and $q_{cyl} \sim 4.2$. From [9, 13].

can be seen, at low density, there is a linear increase in the global energy confinement time (often called Alcator scaling), which saturates at high density, in this case around

Accepted Manuscript

2×10^{20}/m^3. Each point is from an individual discharge, and the ensemble includes a 10% variation of magnetic field and a 25% range of plasma current, which gives rise to the scatter. With the advent of auxiliary heating techniques, global attention turned to the confinement properties of plasmas with external power input. More disappointment ensued as it was found that the energy confinement degraded with increasing input power, dubbed the low confinement mode (L-mode). Happiness was soon restored with the discovery of the high confinement regime (H-mode). Concentration in the 90s was dominated by the study of the energy confinement properties of H-mode, and the Ohmic confinement regimes were largely ignored. In conjunction with improvements in turbulence diagnostics and gyro-kinetic code modeling, the association of the curious rotation reversal phenomenon with the transition between the LOC and SOC regimes [34] has launched a renaissance in the study of Ohmic confinement in the last decade.

Understanding low collisionality regimes in which trapped electron mode (TEM) effects can dominate is relevant for the success of future hot reactor plasmas. The purpose of the present discussion is the documentation of the current understanding of the LOC/SOC transition by bringing to bear all related phenomenology, including gyro-kinetic modeling and a theoretical framework. This ubiquitous and seemingly simple phenomenon has remained largely unexplained for decades, and provides a test bed for theory and simulations. Section 2 will cover the characteristics of the LOC and SOC regimes with a comparison of energy confinement time as a function of density from tokamaks of all different sizes, shapes, operating magnetic fields and plasma currents. In section 3 will be presented features of the rotation reversal and cold pulse temperature inversion phenomena, and the apparent connexion with the LOC/SOC transition observed on many devices. Changes in turbulence across this transition are also catalogued. The current understanding of the LOC and SOC regimes is reviewed in section 4 along with a summary of gyro-kinetic modeling results. Areas for future work will be outlined in section 5.

2. The LOC/SOC Transition

In this section characteristics of the LOC and SOC regimes will be documented, as has been done previously [27]. As a point of reference, consider the recent plot of energy confinement time as a function of density shown in Fig.2 [37]. This series of individual Alcator C-Mod discharges [33, 37] at 5.2 T and 0.81 MA (q_{95} = 4.4) reveals a linear relation in the LOC regime, which saturates $\sim0.8\times10^{20}$/m^3. The linear portion is well fit by the solid line which has a slope slightly larger than the "neo-Alcator" scaling, shown by the dashed line [19] and given by $\tau_{\rm nA}$(ms) = 70 n_e q(a) $\sqrt{\kappa}$ a R^2, with minor and major radii a and R in m and n_e in 10^{20}/m^3. Here κ is the elongation and q(a) is the edge value of the inverse rotational transform, $q_{\rm cyl}$ for limited plasmas and q_{95} for diverted discharges. The slight discrepancy between these two lines indicates that the LOC/neo-Alcator scaling needs to be revisited with the inclusion of contemporary devices. The high density points are in good agreement with the ITER-89P [48] L-mode scaling, $\tau_{\rm 89P}$ (ms) = 48 I$^{0.85}$ R$^{1.2}$ a$^{0.3}$ $\kappa^{0.5}$ B$^{0.2}$ A$^{0.5}$ $\bar{n}_e^{0.1}$ P$^{-0.5}$ (with I in MA, B in T and A, the atomic mass of the background ion, in AMU), shown by the dash-

Accepted Manuscript

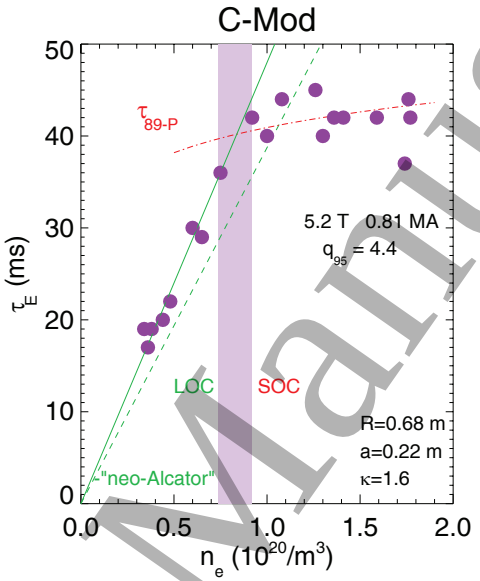

Figure 2: The global energy confinement time as a function of average density for individual 5.2 T, 0.81 MA (q_{95} = 4.4) C-Mod discharges. The solid line is the best fit in the LOC regime while the dashed line represents the "neo-Alcator" scaling. The dash-dot line in the SOC regime indicates the ITER-89P L-mode scaling. From [37].

Accepted Manuscript

dot line. For these deuterium discharges, the Ohmic input power, P, was around 0.9 MW. (The ITER-89P scaling is usually used for auxiliary heated L-mode plasmas, and works here presumably since $P_{oh} = I_p V_{loop}$ with only a weak dependence of resistivity on density.) From τ_E *versus* n_e diagrams it is difficult to pin down the precise critical density between the LOC and SOC regimes but it is safe to say that it falls within the vertical band in this case. A more exact determination comes from rotation reversals and turbulence measurements observed on several devices, which will be discussed in the next section.

Once Ohmic confinement saturation was discovered, it was soon realized that the critical density depends upon the plasma current [7, 14, 20, 29, 34, 37, 38, 40, 44]. An early example of this effect is shown in Fig.3, a comparison of τ_E as a function of $\bar{n}_e$ for various plasma currents at fixed magnetic field for DIII discharges [14]. The con-

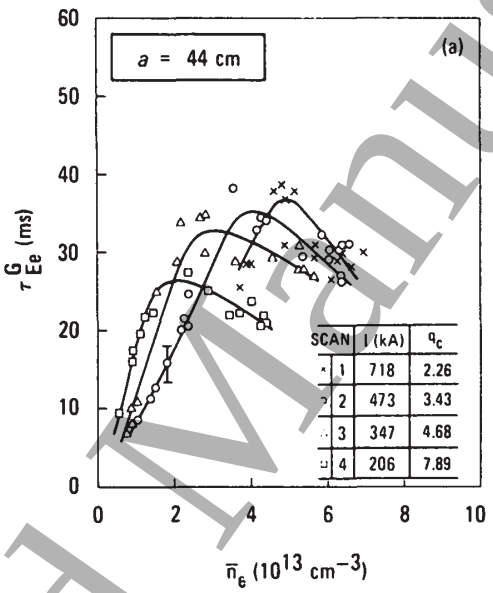

Figure 3: Global energy confinement times as a function of average electron density for DIII deuterium plasmas at 2.4 T for different plasma currents. $\times$s: 0.72 MA; dots: 0.47 MA; triangles: 0.35 MA; squares: 0.21 MA. From [14], used with permission.

finement saturation density is seen to increase at higher I_p. This effect is summarized in Fig.4 which shows the LOC/SOC critical density as a function $1/q_{95}$ ($\propto I_p$) for 5.4 T C-Mod plasmas obtained from a series of τ_E *vs.* n_e scans with varying plasma current [37, 38]. These results are consistent with $n_{crit} \propto 1/q_{95}$ as $n_{crit} q_{95} = 3.6$, shown by the solid line and similar to earlier results [49]. $n_{crit} q_{cyl} = 3$ was found for 6 T FTU discharges [26]. From a comparison of Figs.2 and 3 it is evident that the LOC/SOC critical density is lower in DIII (R = 1.43 m) than it is in C-Mod (R = 0.68 m). The size scaling of the LOC/SOC transition can be determined from a comparison of ob-

Accepted Manuscript

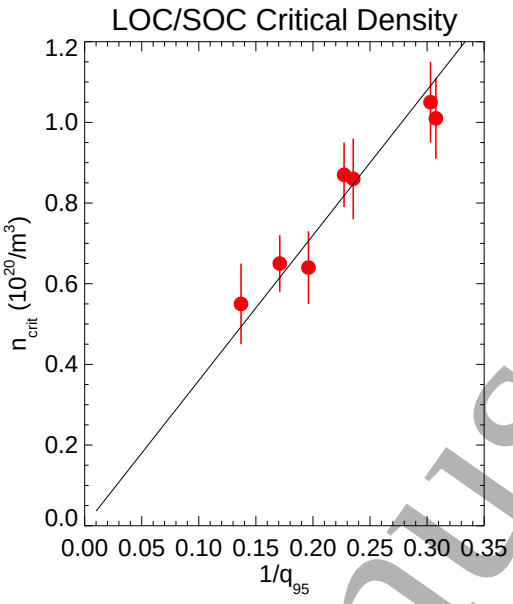

Figure 4: The LOC/SOC critical density as a function $1/q_{95}$ ($\propto I_p$) for 5.4 T C-Mod discharges. The line represents $n_{crit} q_{95} = 3.6$.

servations from a large number of devices. Shown in Fig.5 is the critical density as a function of major radius R for several tokamaks, with edge q values between 2.8 and 3.8 [37]. These points are consistent with a 1/R scaling, shown by the solid line, suggesting that the LOC/SOC transition occurs with $n_{crit} q(a) R \approx$ constant. There is some deviation from this scaling; for example, ISX-A and FTU have about the same major radius, while there is more than a factor of two difference in the critical density. This could be an indication that other parameters are important, and this will be discussed in the next section. The product nqR = constant supports the notion of a critical collisionality [37], since the ratio of the collision frequency to the bounce frequency $\equiv \nu_*$ $\approx 0.0118 n_e q R Z_{eff}/T_e^2 \epsilon^{1.5}$ (with R in m, n_e in 10^{20}/m^3 and T_e in keV) [50]. For C-Mod Ohmic plasmas, the ratio of Z_{eff}/T_e^2 is only very weakly dependent upon density and is independent of q_{95} at the critical density [37, 38] (see Fig.33c). All devices show Z_{eff} and T_e falling together with increasing density. An alternative collisionality ν_{eff}, the ratio of the collision frequency to the curvature drift frequency [51, 52], should also be considered. This is discussed in detail in section 5.

3. Rotation Reversals and Turbulence Changes

There are several shortcomings in the study of the LOC/SOC transition due to the

Accepted Manuscript

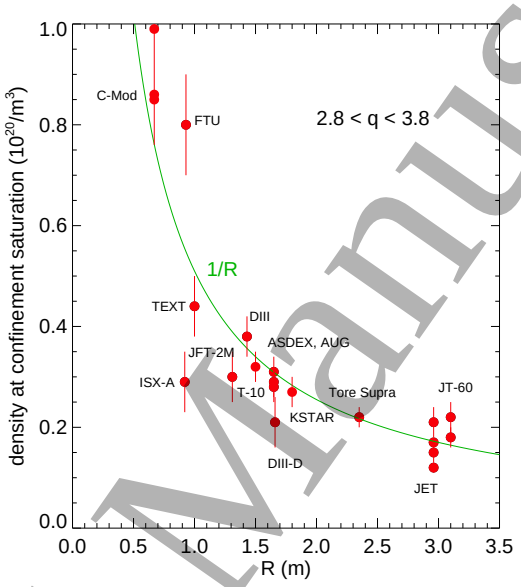

Figure 5: The critical density at confinement saturation as a function of major radius from a variety of tokamaks with plasmas having q(a) between 2.8 and 3.8. The line is proportional to 1/R. From [37].

Accepted Manuscript

very nature of the dependence of the global energy confinement time as a function of density with other parameters held fixed. The first issue is that detecting a change in slope of the confinement is not a precise metric; examination of Figs.1-3 reveals that the critical density is somewhat blurry. Other deficiencies are that there are no details on the transition dynamics or any information on where across the plasma profile this process is being driven. There is growing evidence that other changes occurring at the LOC/SOC transition, such as intrinsic rotation reversals and modification of turbulence characteristics, can shed light on the underlying mechanism. The case that Ohmic confinement saturation and rotation reversals are related [34, 35, 37, 38, 44, 47] is supported by Fig.6 which compares global energy confinement times and core rotation velocities as a function of density for individual 5.4 T C-Mod discharges at three different plasma currents. There is in no way any causality implied in this relation-

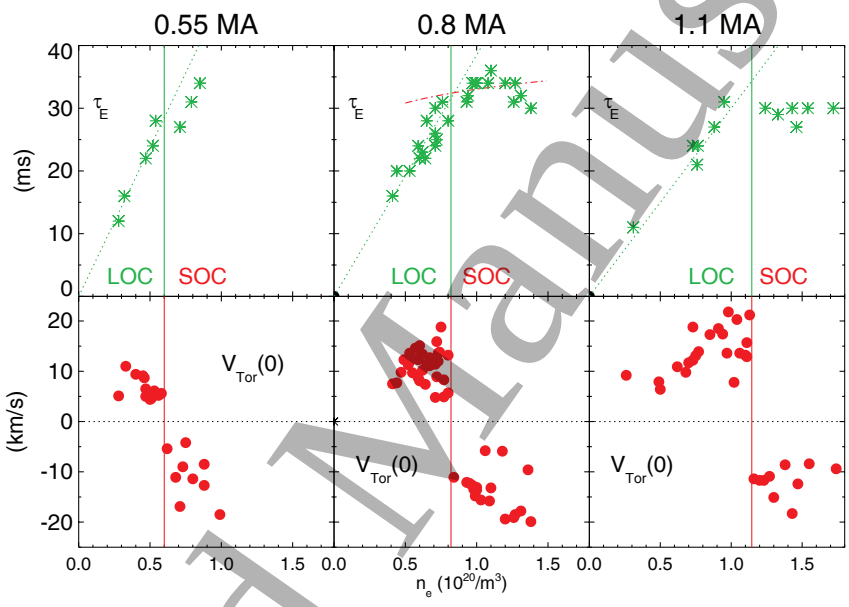

Figure 6: Top: energy confinement times for 0.55 MA (left), 0.8 MA (center) and 1.1 MA (right) shot by shot density scans at fixed magnetic field. Bottom: corresponding core rotation velocities. Vertical lines are from the rotation reversal critical densities. For energy confinement times, green dotted lines indicate Alcator scaling in the LOC regime, and for the 0.8 MA case, the red dash-dot line represents the ITER-89P L-mode scaling.

ship. While the precise LOC/SOC density is a bit fuzzy (changes in slope are not well defined), there is no question about the critical rotation reversal density, since the core velocity changes sign. The reversal density is very sharp, at $0.60\times10^{20}/\mathrm{m}^3$ for the 0.55 MA discharges, $0.81\times10^{20}/\mathrm{m}^3$ for 0.8 MA and $1.14\times10^{20}/\mathrm{m}^3$ for 1.1 MA. These values, shown by the vertical lines, are in good qualitative agreement with the

Accepted Manuscript

confinement saturation, although the confinement saturation is not so distinct in the lowest current case. The relation between the two phenomena is further emphasized in Fig.7 which shows the LOC/SOC and rotation reversal critical densities as a function of plasma current for C-Mod discharges at fixed magnetic field (5.2-5.4 T). The line

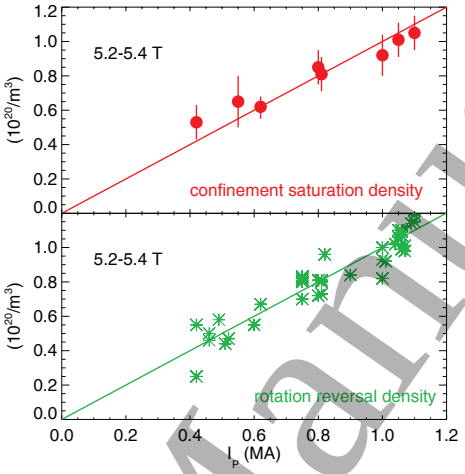

Figure 7: The transition density between the LOC and SOC regimes (top) and the critical density for core toroidal rotation reversals (bottom) as a function of plasma current for fixed magnetic field. The lines have the same slope. From [34].

in the bottom frame from the best fit to the rotation reversal points matches very well to the energy confinement data in the top frame. There are many more rotation reversal points since the reversal density can be determined from a single discharge with a very slight density ramp, whereas τ_E *versus* density plots require several discharges in a shot by shot density scan (unless there is a relatively slow density ramp in a long discharge, such as has been done in AUG [23], Tore Supra [40] and DIII-D [47]). The connexion between the LOC/SOC transition and rotation reversals may be coincidental due to interdependencies on some plasma parameters, such as the density profile and the current, which affect the collisionality, impurity content and electron-ion coupling. The LOC/SOC transition on AUG has been explained by changes in ITG mode stability through a variety of actuators [53], to be discussed in detail in section 4. Rotation

Accepted Manuscript

reversals on AUG have been modeled by a completely different phenomenon, a kinetic electron effect, due to density profile curvature [54].

With these *caveats*, if rotation reversal can be used as a proxy for Ohmic confinement saturation, it enables a probe of the LOC/SOC transition dynamics, as well as revealing radial profile information. The former point is demonstrated in Fig.8 which shows core rotation reversals in response to density modulation for a 1.05 MA, 5.4 T C-Mod discharge [34]. As the density is ramped down through $0.98\times10^{20}/\mathrm{m}^3$, the central rotation begins to change from the counter-current direction at 0.67 s, going from ~ -18 km/s to $\sim +10$ km/s by 0.75 s. This process repeats itself in the opposite direction when the density is ramped back through $1.07\times10^{20}/\mathrm{m}^3$ with the second reversal beginning at 1.15 s. There is no change in the rotation at r/a = 0.75 (dashed line) during the core reversal. The reversal cycle transpires with a 10% change in the electron density. The hysteresis [55, 34, 56, 57] of this process, which is *prima facie* evidence of a bifurcation, is shown in Fig.9, and reiterates how sensitive rotation reversals are to the

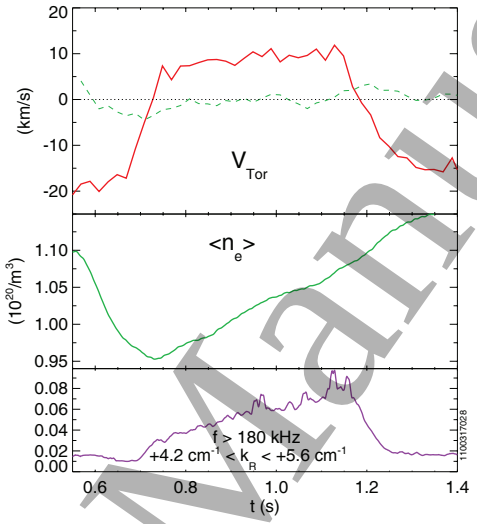

Figure 8: Time histories of the toroidal rotation velocity (top frame) in the plasma center (solid line) and at r/a = 0.75 (dashed line), average electron density (middle frame) and core density fluctuation intensity (bottom frame) for a 1.05 MA, 5.4 T (q_{95} = 3.2) C-Mod discharge which underwent two core rotation reversals.

Accepted Manuscript

electron density. This allows precise determination of the critical density compared to

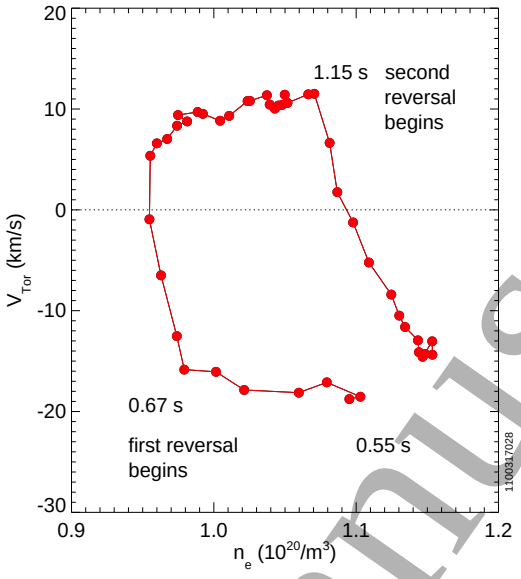

Figure 9: The discharge trajectory in the n_e-V_{Tor} plane for the C-Mod plasma of Fig.8. Points are separated by 20 ms. From [34].

that obtained from changes in slope in τ_E *vs.* density diagrams. If one does not believe rotation reversals and confinement saturation are related, then the LOC/SOC density will remain ill defined, as in Fig.2. Note that the core rotation reversal transpires on a time scale similar to the energy confinement time (10s of ms), but much faster that the current relaxation time, several 100s of ms.

While the dependence of the LOC/SOC transition on density and current is well established, scant information is available on the relation to the magnetic field. On the other hand, rotation reversals are known to exhibit similar hysteresis from B_T ramps as was demonstrated with density [34]. Shown in Fig.10 is a comparison of two C-Mod discharges, one with a magnetic field modulation and the other without. For these 0.8 MA plasmas with constant densities $\sim 0.9\times10^{20}/m^3$, the rotation velocity is seen to reverse when the magnetic field falls below 3.6 T and reverses again at 3.7 T. Corresponding critical values of q_{95} were 2.95 and 3.05, respectively. If the LOC/SOC transition is related to rotation reversals, this provides important information about the role of the magnetic field.

Another phenomenon which might be related to the LOC/SOC transition and rotation reversals is the so-called "non-local" cut-off; the critical density where the non-diffusive core response to edge cold pulses disappears [58, 59, 60, 61, 38, 62]. This association is shown in Fig.11 for 5.4 T, 0.8 MA C-Mod discharges. As can be seen in the second panel, at densities below $0.80\times10^{20}/m^3$ the response to an edge cool-

Accepted Manuscript

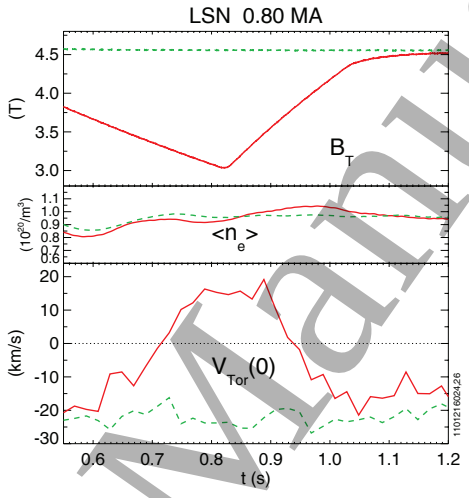

Figure 10: Time histories of 0.8 MA LSN discharges with (solid) and without (dashed) a magnetic field ramp. From top to bottom, the toroidal magnetic field, the electron density and the central toroidal rotation velocity.

Accepted Manuscript

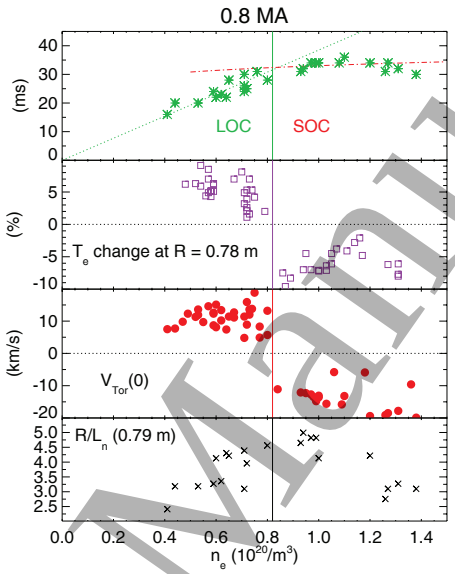

Figure 11: The global energy confinement time (top), percent change in electron temperature at R = 0.78 m following impurity injections (second frame), core toroidal rotation velocity (third frame) and the inverse density gradient scale length (fourth frame) as a function of electron density for individual 0.8 MA, 5.4 T discharges.

Accepted Manuscript

ing is an increase in the interior temperature (the "non-local" effect) whereas above $0.85\times10^{20}/m^3$ the core response is diffusive, with a drop in the core temperature. The temperature at R = 0.78 m is shown, which is just inside of the temperature inversion point (see Fig.12). The critical cut-off density coincides very nicely with the rotation reversal and LOC/SOC transition density for C-Mod discharges. However, for AUG plasmas, the connexion is less clear. The association between the LOC/SOC transition and cold pulse inversion cut-off may be coincidental through inter-related plasma parameter dependences. The electron density gradient at the mid-radius appears to peak near the critical density as seen in the bottom frame, and will be discussed in section 4.

Examination of the profiles of the rotation and temperature reveals important information about spatial dependence which might possibly be relevant to the LOC/SOC transition. Shown in the top of Fig.12 are rotation velocity profiles on either side of a dynamic rotation reversal induced by a density ramp in a 5.4 T, 0.8 MA (q_{95} = 4.1) C-Mod discharge [38]. At low density in the LOC phase, the rotation is co-current with

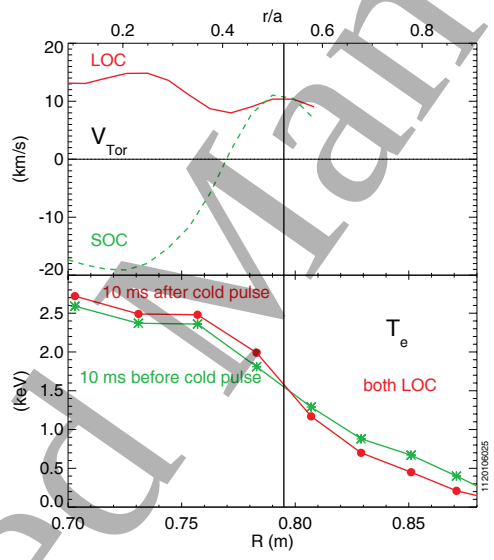

Figure 12: Top frame: rotation velocity profiles at two different times for a discharge with a dynamic rotation reversal. Bottom frame: electron temperature profiles 10 ms before (green asterisks) and 10 ms after (red dots) an edge cold pulse during the LOC phase of the same discharge. The solid vertical line shows the rotation velocity profile anchor point.

Accepted Manuscript

a relatively flat profile shape. At higher density with SOC, the profile is hollow, with counter-current rotation in the core. There is no change in the profile outside of the mid-radius across the core reversal, as was seen in Fig.8. This velocity profile behavior is widely observed in rotation reversals [55, 63, 64, 34, 36, 38, 39, 44, 65, 45, 66, 46, 47, 56]. Further evidence that the non-diffusive temperature inversion cut-off and rotation reversals are connected comes from inspection of the electron temperature profiles in the bottom frame of Fig.12. These were from the LOC phase of the same discharge, taken just before and just after an edge cold pulse [38]. After the pulse, the temperature at the edge is seen to drop while that in the center actually increases. The temperature flex point near the mid-radius coincides with the rotation reversal anchor point. That this is not a coincidence is supported by Fig.13 which compares these two critical radii as a function plasma current ($\propto 1/q_{95}$) for individual 5.4 T C-Mod discharges [38]. Both the rotation reversal anchor point and the electron temperature flex point move

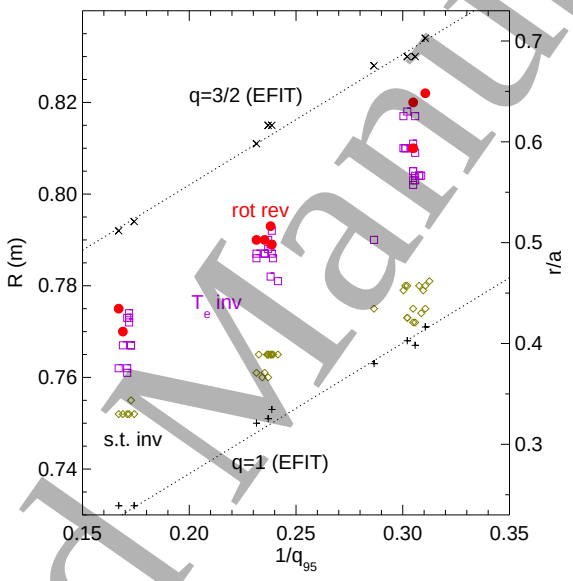

Figure 13: Radial locations of the q=3/2 surface ($\times$s), rotation reversal anchor point (dots), electron temperature profile flex point (boxes), sawtooth inversion radius (diamonds) and q=1 surface (plus signs) as a function of $1/q_{95}$. From [38].

radially outward together as the plasma current is raised (or q_{95} is reduced). The relation between the reversal anchor point and the plasma current has also been seen on TCV [63] and KSTAR [66]. These critical radii are near the steepest gradient location on the electron temperature profile and fall between the q=1 and q=3/2 surfaces. When trying to explain the LOC/SOC transition it might be important to consider what is special about this radius in the plasma.

All available information about the critical density for the LOC/SOC transition,

Accepted Manuscript

rotation reversals and thermal non-diffusive cut-off have been combined in Fig.14, a plot of the product of n_{crit}, R and the edge q value, as a function of toroidal magnetic field for a large number of tokamaks. This contains all the points from Fig.5, expanded

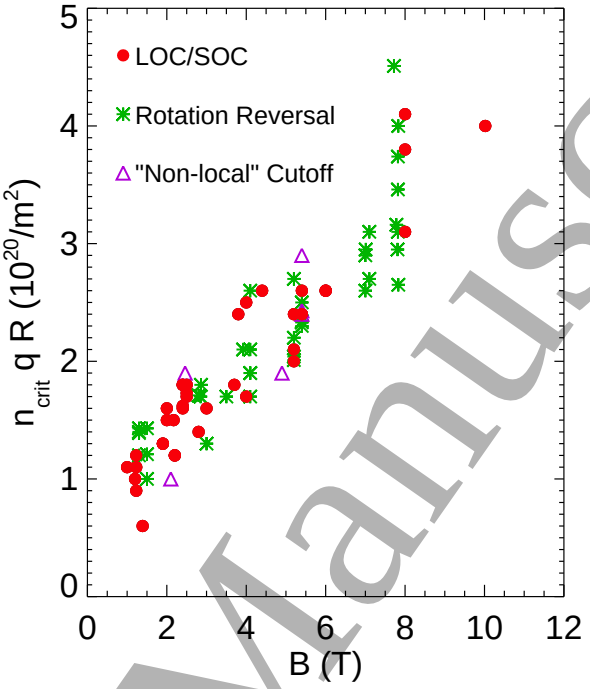

Figure 14: The product of n_{crit}, the edge q value and R as a function of toroidal magnetic field from 18 individual tokamaks. Red dots are from the LOC/SOC transition, green asterisks are from rotation reversals and purple triangles are from the "non-local" cut-off.

to include all published edge q values. The LOC/SOC points represent contributions from 16 individual devices, whereas the rotation reversal and temperature inversion cut-off points are from five and four tokamaks each, respectively. The n_{crit}qR product scales linearly with magnetic field strength and probably explains some of the scatter apparent in Fig.5. Various machine entries are summarized in Table 1.

There is still $\sim$25% scatter for a given magnetic field in Fig.14, suggesting that there are other hidden variables, such as impurity content or electron to ion temperature ratio. Likely these hidden parameters are related to either TEM stabilization or ITG mode destabilization. This dependence does not appear to be related to the Greenwald density limit or MHD disruption limits since the values of the density are quite low. Fig.14 can be used for predicting the LOC/SOC critical density in future devices. For

Accepted Manuscript

Device	R (m)	L/S	rot. rev.	"n-l"	[Ref.]
Alcator C	0.64	x			[9, 13]
ASDEX	1.65	x			[23]
AUG	1.65	x	x	x	[28, 61, 36, 39]
C-Mod	0.67	x	x	x	[33, 34, 35, 37, 38, 62]
DIII	1.43	x			[14]
DIII-D	1.63	x	x		[30, 47]
FT	0.83	x			[12]
FTU	0.93	x			[26]
ISX-A	0.92	x			[7]
JET	2.95	x			[29]
JFT-2M	1.29	x			[20]
JT-60	3.1	x			[20]
KSTAR	1.8	x	x		[44, 45, 66]
RTP	0.72			x	[59, 60]
T-10	1.5	x			[31]
TCV	0.88		x		[55, 63, 64]
TEXT	1.0	x			[24]
TFTR	2.36			x	[58]
Tore Supra	2.35	x			[25, 40]

Table 1: Various device contributions to Fig.14 (major radius R listed) from the LOC/SOC transition, rotation reversals and "non-local" cut-off.

Accepted Manuscript

ITER operation at 5.3 T, the nqR product is expected to be around 2.5, which yields a critical density of 0.1×10^{20}/m^3 with R = 6.2 m and q_{95} = 3.5. For ARC (R = 3.3 m) [67] at 9.2 T and q_{95} = 3.5, the expected density is 0.3×10^{20}/m^3, whereas for SPARC [68] at 12 T, the product from Fig.14 is about 5, and with R = 1.85 m and q_{95} = 3.5, the predicted density is 0.8×10^{20}/m^3. For JT-60SA [69], with B_T = 2.25 T, R = 2.96 m and q_{95} = 3.5, the critical density is estimated to be $\sim0.1\times10^{20}$/m^3 and for DTT [70] (B_T = 6 T, R = 2.2 m and q_{95} = 3.5) the value is $\sim0.4\times10^{20}$/m^3. As a note, if reactors are chosen to operate in H-mode, the target plasmas will be in the SOC regime, otherwise the power threshold will be too high.

The final piece of the LOC/SOC puzzle comes from observed changes in turbulence across the transition. There are numerous cases of this from a wide variety of diagnostics [71, 72, 73, 24, 25, 30, 74, 75, 50, 33, 34, 35, 37, 76, 77, 40, 78, 79, 41, 43, 80, 81, 66, 82], including laser scattering, microwave reflectometry, probes and correlation electron cyclotron emission (CECE). An early example using laser scattering is shown in Fig.15 from Tore Supra [25] which compares a shot by shot scan of global energy confinement time (top) and density fluctuation intensity (bottom) as a function of electron density. The fluctuations are large at low density in the LOC regime and decrease

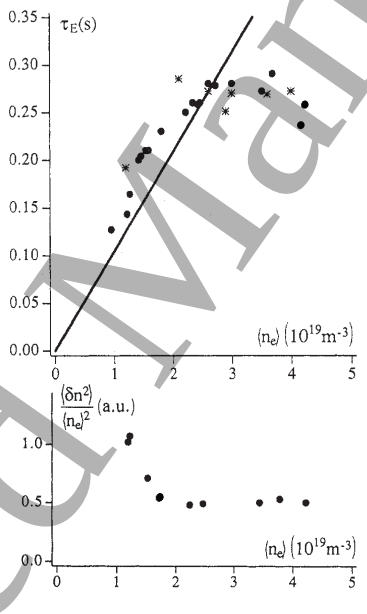

Figure 15: Global energy confinement times (top) and density fluctuation intensities (bottom) as a function of electron density for Tore Supra plasmas. The line in the top frame represents the Alcator scaling. From [25], used with permission.

to a saturated level as the energy confinement also saturates. A complementary example of turbulence changes at lower k is shown in Fig.16 from DIII-D [30], where the fluctuation level is low in the LOC regime and saturates at a higher value with SOC. The

Accepted Manuscript

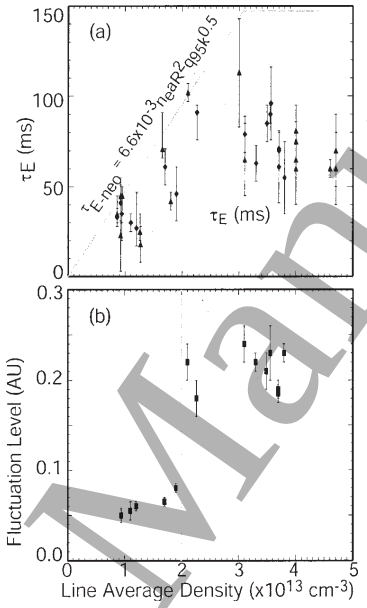

Figure 16: Global energy confinement times (top) and integrated density fluctuation levels at k_θ = 2 cm^{-1} (bottom) as a function of electron density for DIII-D plasmas. From [30], used with permission.

Accepted Manuscript

large transformation in turbulence intensity occurs with a very small variation of density near $2.0\times10^{19}/m^3$, and it is much easier to determine the critical density from this dramatic turbulence intensity increase (bottom frame) than from the change in slope of the energy confinement time (top frame). These two cases demonstrate the correlation between turbulence changes and energy confinement. Further evidence comes from examination of the turbulence propagation direction during a density/collisionality scan and an example of this from AUG plasmas, utilizing microwave reflectometry, is shown in Fig.17 [50]. It is clear that the turbulence propagation direction (red dots) at r/a = 0.7

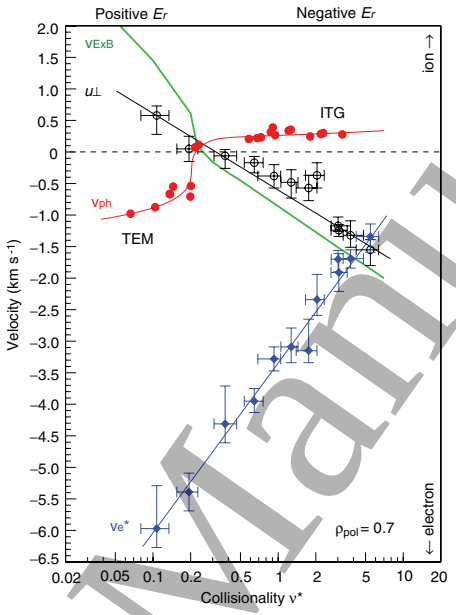

Figure 17: Measured core turbulence propagation velocity $u_\perp$ (black circles), computed turbulence phase velocity v_{ph} (red dots), extracted $\mathbf{E}\times\mathbf{B}$ velocity (green line) and measured electron diamagnetic velocity v_{e*} (blue diamonds) as a function of collisionality at r/a $\sim$ 0.7 for AUG Ohmic plasmas. From [50], used with permission.

switches at a precise value of collisionality $\nu_* = 0.25$. Flips in the turbulence propagation direction have also been observed on Alcator C [72], MAST [78] and Tore Supra [81]. A change in the turbulence propagation direction, and the concomitant change in sign of the residual stress, is one way to explain the rotation reversal phenomenon [34, 35, 37]. The residual stress is the component of the momentum flux which is neither dependent on the momentum diffusivity nor the momentum convection [83]. Nonlinear global effects appear to be at the heart of the changes in the residual stress [47]. This is discussed in detail in the next section.

The relation between turbulence changes and rotation reversals has been studied extensively on C-Mod. An example of chord integrated spectrograms of density fluctuations from a laser scattering diagnostic in both the SOC and LOC regimes is shown in

Accepted Manuscript

Fig.18 [35]. The presence of high frequency, high wavenumber lobes is evident during

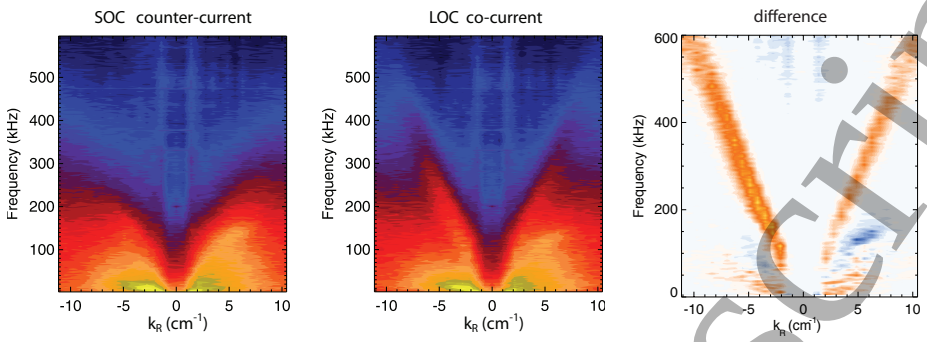

Figure 18: Dispersion plots S(k,f) of turbulence before (0.608 s, counter-current rotation, SOC, left panel) and after (0.859 s, co-current rotation, LOC, middle panel), and the difference between the two (right panel) for the first rotation reversal of the C-Mod discharge shown in Fig.8. From [35].

the LOC phase (as isolated in the right panel) for 5.4 T discharges with plasma currents above 0.9 MA. These features have the same slope for positive and negative k, therefore originate from inside r/a = 0.7 where the flux surfaces are up/down symmetric, and from the slope indicate a poloidal phase velocity of $\sim$3.8 km/s. In fact the intensity of these lobes is well correlated with the LOC co-current rotation state [34, 35] as can be seen in the bottom panel of Fig.8. This demonstrates the extreme sensitivity of both the core rotation and high k density fluctuation level to the LOC/SOC transition. Perhaps the most common signature of density fluctuations only present in the LOC regime comes from microwave reflectometry diagnostics. A typical example is shown in Fig.19 from Tore Supra plasmas [40]. Distinct features near $\pm$50 kHz (here called QC modes) are visible only in the LOC regime, which extends to higher density at higher plasma current. These QC modes will be discussed in detail in the next section. Similar microwave spectral characteristics have been observed on TEXTOR [74, 79, 43], T-10 [75], C-Mod [34], Tore Supra [40, 41, 43, 80], JET [43] and KSTAR [66, 82].

All of the turbulence measurements mentioned above were of density fluctuations. Changes in measured electron temperature fluctuations from CECE have also been observed across the the LOC/SOC transition, and an example from C-Mod is shown in Fig.20 [77]. There is a distinct feature near 50 kHz which is only present in LOC plasmas.

A summary of turbulence measurements from various techniques on different devices is given in Table 2, which includes wave number and frequency ranges, and values of $k_\perp \rho_s$ for any noticeable features. With one exception, all observations are of density fluctuations. Most devices exhibit turbulent features with $0.1 < k_\perp \rho_s < 0.7$. A commonality of many observations is the presence of prominent turbulent features in the LOC regime which disappear following the switch to SOC, and a change in the

Accepted Manuscript

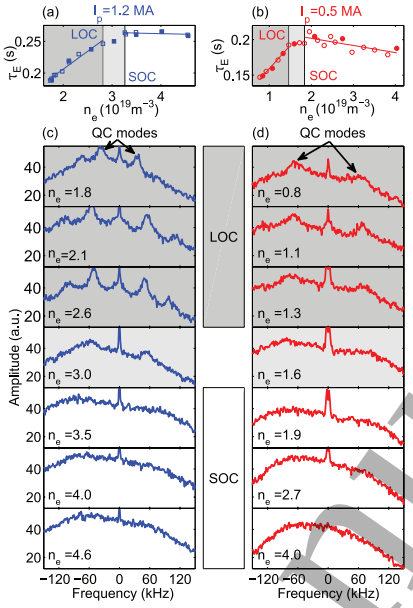

Figure 19: Tore Supra reflectometry spectra during LOC/SOC transitions achieved at 3.8 T by scanning the central line averaged density (10^{19}/m^3), for plasma currents of 1.2 MA (left) and 0.5 MA (right). In the top frame are the global energy confinement times as a function of electron density. From [40], used with permission.

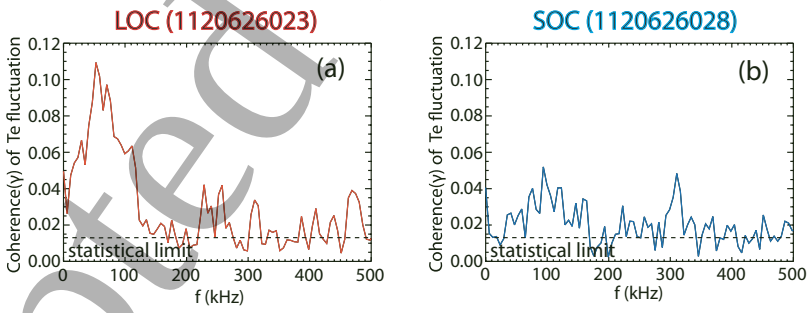

Figure 20: Coherence of electron temperature fluctuations for C-Mod LOC (left) and SOC (right) plasmas. From [77], used with permission.

Accepted Manuscript

Device	tech.	k (cm^{-1})	ν (kHz)	$k_\perp \rho_s$	notes	[Ref.]
Alcator C	laser	1-20	30-150	0.13-0.4	dir. flip at LOC/SOC	[72]
TEXT	laser	4-12	40-500	0.1-0.4	ion mode in SOC	[73, 24]
Tore Supra	laser	6	50-500	–	LOC	[25]
DIII-D	laser	2	50	0.2-0.5	ion mode in SOC	[30]
TEXTOR	μwave	1-3	50-150	0.3-0.5	QC mode in LOC	[74, 79, 43]
T-10	μwave	–	70-250	0.3-0.7	QC modes in both	[75]
AUG	μwave	–	–	$<$0.1	dir. flip at LOC/SOC	[50]
C-Mod	laser	1-5	20-25	–	SOC	[33]
C-Mod	laser	2-10	50-400	0.15-0.7	lobes in LOC	[34, 35, 38]
TEXTOR	probes	–	–	–	residual stress in LOC	[76]
C-Mod	CECE	–	50	$<$0.3	T_e fluctuations in LOC	[77]
Tore Supra	μwave	1	30-120	$<$0.4	QC mode in LOC	[40, 41, 80]
MAST	μwave	–	–	10	direction flip	[78]
JET	μwave	–	80-120	–	QC mode in LOC	[43]
Tore Supra	μwave	–	–	–	dir. flip at LOC/SOC	[81]
KSTAR	μwave	–	30	–	QC mode in LOC	[66, 82]

Table 2: Turbulence measurements from various techniques on listed devices, with wavenumber k and frequency ν ranges, and $k_\perp \rho_s$ values for notable features.

turbulence propagation direction across the LOC/SOC transition. As will be seen in the next section, these features in the LOC regime are connected with TEMs, which is consistent with a larger trapped electron fraction at lower collisionality. There is very little information available on changes in edge fluctuations across the LOC/SOC transition.

4. Comparison with Gyro-Kinetic Modeling and Theory

The first attempt to describe LOC confinement considered filamentation of the toroidal plasma current on rational flux surfaces with the mixing length given by the skin depth [84]. Following treatments to explain the "Alcator" scaling (the LOC regime) centered on the effects of dissipative trapped electron modes at low ν_* [85]. Since the trapped electron fraction decreases as the collisionality is raised, eventually 'η_i' or ion temperature gradient (ITG) modes dominate, causing the confinement to saturate (the SOC regime) [85]. A two fluid transport model, including MHD effects, was found to capture the observed scalings of energy confinement time *versus* density on Alcator A, DIII, Alcator C and PDX [85]. An example is shown in Fig.21 from DIII. The calculated points (open circles) agree with the observations (black dots), both in the linear and saturated regimes. Recent treatments using modern gyro-kinetic codes reach similar conclusions [47]. To demonstrate that ITG modes are responsible for the confinement saturation, the straight line marked 'b' indicates the calculated scaling

Accepted Manuscript

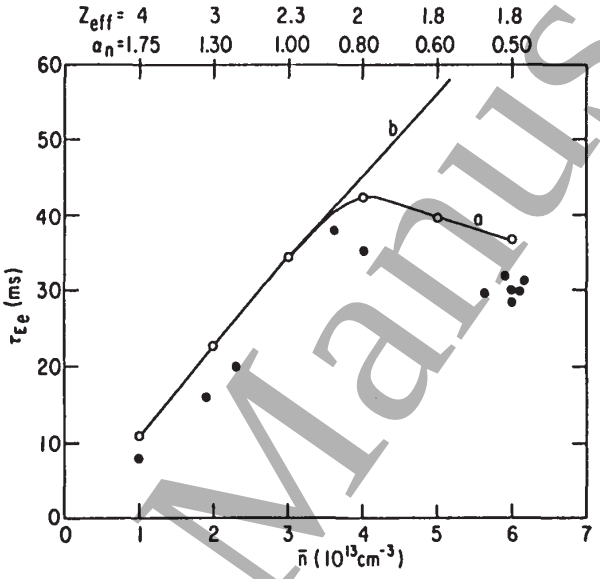

Figure 21: Electron energy confinement time *versus* density for DIII plasmas. The black circles are the experimental results and the open circles (and curve a) are the results of the transport code. Curve b represents the results with η_i modes turned off. From [85], used with permission.

Accepted Manuscript

without the ITG/η_i modes. This 'restoration' of LOC at high density is reminiscent of the improved Ohmic confinement (IOC) regime observed on ASDEX [23] and also seen in Alcator C with pellet injection [17]. In both cases it is the peaking of the density profile and decrease of impurity content which stabilizes ITG modes, preventing the confinement saturation. The increase in density peaking, when near the ITG-TEM transition, could indeed suppress ITG modes (since it drives TEMs, and near the transition, the two modes compete), but in general, with kinetic electron ITG modes present, the density gradient also destabilizes ITG modes.

Increasing the collisionality has other effects besides just reducing the trapped electron fraction: electron-ion coupling increases, and it is universally observed that the impurity content $Z_{\rm eff}$ decreases (see Fig.33b), which reduces ion dilution. These latter effects play a role in ITG mode stability, modifying the thermal conductivity and thereby affecting energy confinement [86, 42, 87, 53]. An example of this is shown in Fig.22 from AUG [53] where the calculated density scaling of energy confinement time (left) and inverse density gradient scale length (right) for different impurity content are compared with observations. For low $Z_{\rm eff}$, the simulations capture the energy confinement saturation and profile peakedness very well, while for higher $Z_{\rm eff}$ the confinement saturation is lost. This effect has been directly observed using nitrogen gas puffing in C-Mod discharges [42].

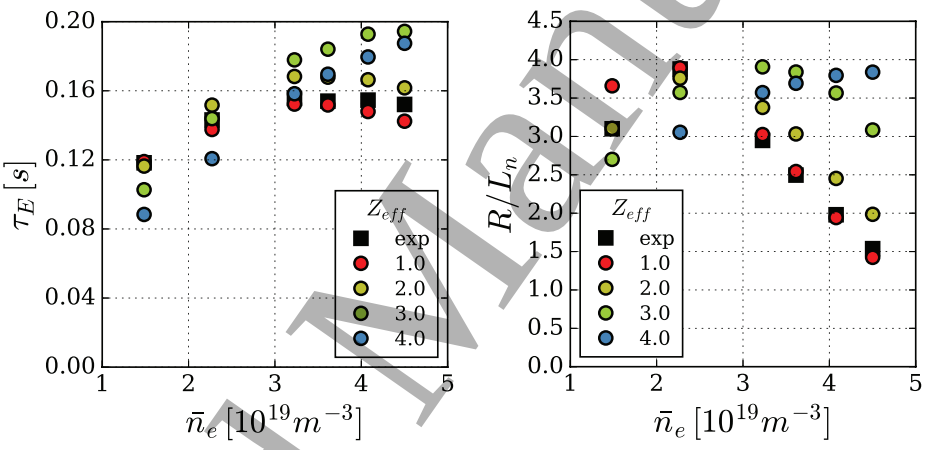

Figure 22: Energy confinement time τ_E and the normalized logarithmic electron density gradient R/L_n averaged within radial range r/a = 0.4 − 0.6 as functions of average electron density, for different $Z_{\rm eff}$ values. From [53], used with permission.

Over the years numerous gyro-kinetic simulations have been performed with an eye towards understanding the LOC/SOC transition [25, 30, 50, 33, 36, 37, 86, 77, 39, 62, 40, 41, 42, 43, 80, 87, 45, 66, 53, 82, 54]. An early example from DIII-D [30] is presented in Fig.23 which shows the calculated radial profiles of growth rates and real frequencies of the most unstable mode at $k_\theta = 2\ {\rm cm}^{-1}$ for LOC (top) and SOC (bottom) conditions. Positive (negative) frequencies indicate electron (ion) modes. Clearly ITG

Accepted Manuscript

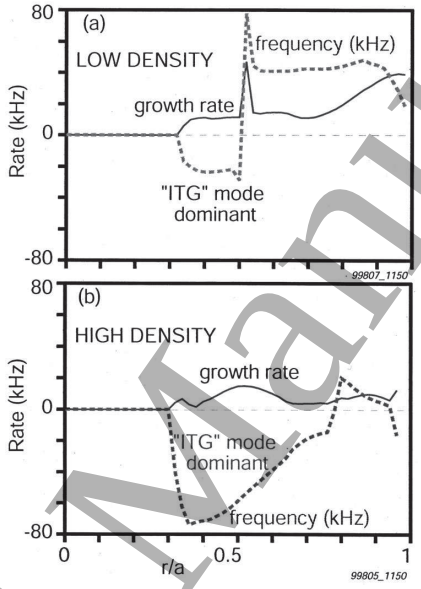

Figure 23: Comparison of the real frequency (dashed line) and growth rate (solid line) of the most unstable mode at $k_\theta = 2\ cm^{-1}$ calculated for low (LOC, upper panel) and high (SOC, lower panel) density DIII-D discharges. From [30], used with permission.

Accepted Manuscript

modes dominate over most of the profile in the SOC regime while TEMs are important with LOC for these DIII-D plasmas. Related linear calculations have been performed for Tore Supra discharges [40, 87] at fixed radius over a large range of wavenumbers. Real frequencies (left) and growth rates (right) are shown in Fig.24 for the LOC (blue) and SOC (red) regimes as a function of $k_\theta \rho_i$. In the SOC regime ITG modes domi-

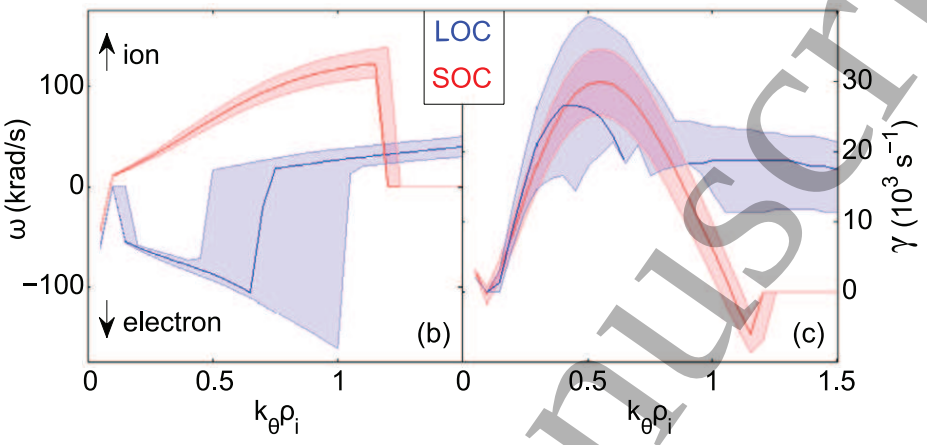

Figure 24: Output of the GENE linear stability analysis of the Tore Supra deuterium discharge #48102 performed at r/a = 0.37 (B_T = 3.7 T and I_p = 1 MA). Calculations are done for two values of the central line average density in the LOC (blue, n_e = 1.66×10^{19}/m^3) and the SOC regime (red, n_e = 3.13×10^{19}/m^3). From [40, 87].

nate for $0.2 < k_\theta \rho_i < 2$ (main ion ITG modes for $k_\theta \rho_i < 0.8$, then carbon ITG modes above that) whereas with LOC, TEMs are important for $k_\theta \rho_i < 0.6$. Non-linear simulations reveal more details about the underlying modes. Fourier decomposition of the frequency spectra for the same Tore Supra discharge is shown in Fig.25 [87]. It is very clear that in the LOC regime the modes with $k_y \rho_s$ between 0.1 and 0.6 propagate in the electron direction, while with SOC they are ion directed. The dominant mode in the LOC regime is very sharply peaked with $k_y \rho_s \sim 0.3$. These simulations have been used to calculate synthetic reflectometer spectra for comparison with experiment [80, 87] and an example is shown in Fig.26. The observed reflectometer spectra are shown on the right for the LOC (top) and SOC (bottom) regimes for comparison with the synthetic spectra on the left. The simulations capture both the sharp QC mode features with LOC and the broadband nature with SOC.

The common story that emerges from the majority of the gyro-kinetic simulations listed above is that TEMs dominate deep in the LOC regime and that ITG modes are dominant with SOC. However, both types of turbulence are present in both regimes, so a more nuanced framing of the problem is appropriate [47]. Under conditions of coexistence of both mode types, it is important to understand the interplay between the two [88] and the conditions for dominance by either. A recent study has considered different turbulence families and sub-dominant modes on either side of a C-Mod rota-

Accepted Manuscript

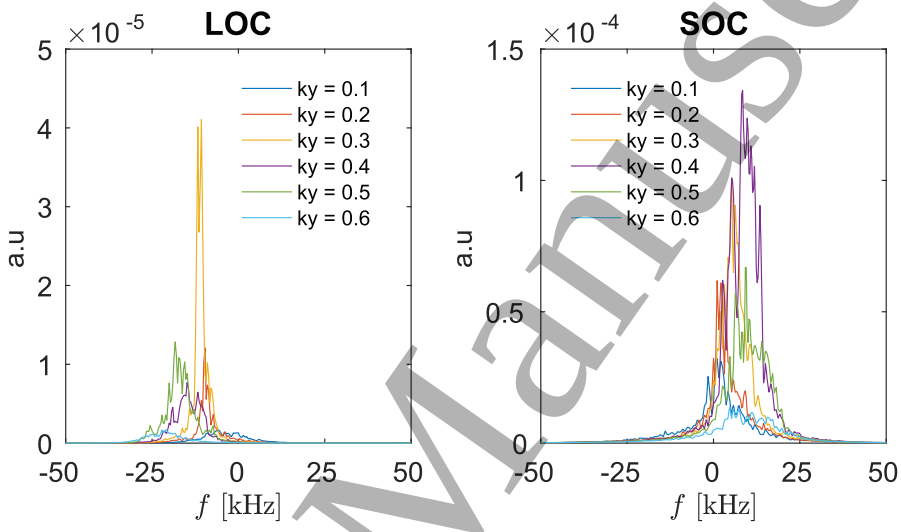

Figure 25: Fourier decomposition (in the binormal coordinate) of the frequency spectra for the LOC phase (left panel) and the SOC phase (right panel) density fluctuations on Tore Supra, averaged over ∼2 ms during the quasi-stationary saturated state of the non-linear simulation, corresponding to over 100 turbulence autocorrelation times. k_y is normalized to $1/\rho_s$. From [87].

Accepted Manuscript

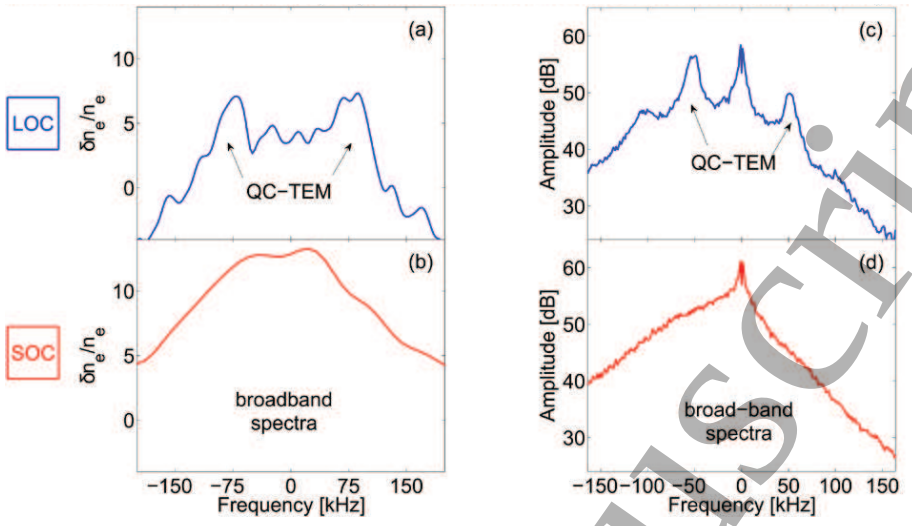

Figure 26: Fluctuation spectra from Tore Supra discharge #48102 provided by a synthetic reflectometer diagnostic (left) using the non-linear gyrokinetic simulations as an input. They are computed at r/a = 0.37 in the LOC (top) and SOC (bottom) regimes. For comparison on the right are the measured spectra. From [80, 87].

tion reversal induced by a very slight density ramp [56, 57]. A reduced model has been constructed using a linear mode quasi-linear transport approximation (mQLTA) where turbulent fluxes are calculated by the sum of a quasi-linear mode weight times an intensity (spectral weight) for each linear mode, assuming a non-linear saturation process is at play. By using the ion and electron heat and electron particle fluxes calculated from power balance, it is possible to constrain the mode intensities. The gyro-Bohm normalized weights from CGYRO [89] runs for the LOC and SOC phases of a C-Mod discharge on either side of a rotation reversal are shown in Fig.27. Four mode families in each case are identified. Family I are low k ion directed ITG modes, important for both ion and electron heat transport, separated in (a) and (b) based upon the efficiency (particles exhausted per unit of ion heat exhausted) of particle flux exhaust. Family I is important for ion heat flux. Family II includes marginally stable trapped electron modes with $k_y \rho_s \sim 1$ and are characterized by their inward particle pinch. Family III are high k electron directed ETG modes which exhaust only electron heat flux. The four mode family intensities for the LOC and SOC regimes are shown in Fig.28. In the LOC case, all four mode families are active. Particle flux balance is ensured by a competition between family Ia and family II. Electron heat transport is governed by families II and III, while torque balance is maintained by both TEMs and ITG modes. In the SOC case, only families Ib and III are active. The particle flux is balanced with family Ib, family III dominates electron heat transport and torque balance is governed by family Ib ITG modes. The conclusion here is that sub-dominant TEMs are important

Accepted Manuscript

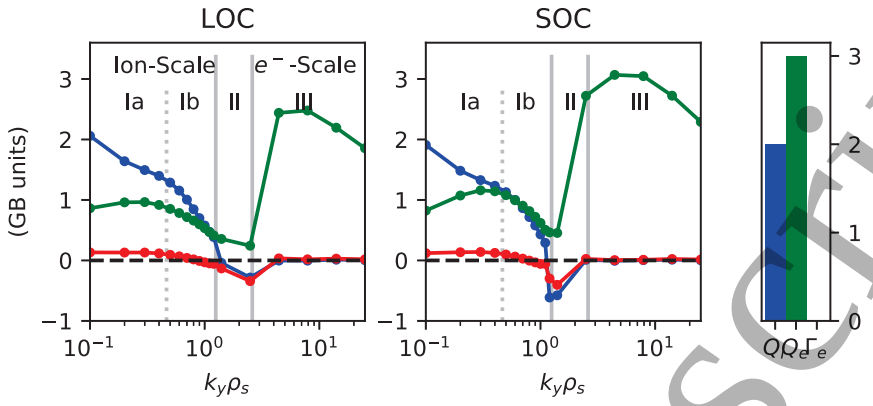

Figure 27: The quasi-linear weights are shown for the most unstable drift wave modes for a range of $k_y\rho_s$ for a 0.8 MA C-Mod plasma in the LOC (left) and SOC (right) phases. The units are gyro-Bohm normalized. The four mode families are labeled Ia, Ib, II and III. The anomalous ion and electron heat fluxes, as well as the electron particle flux, are shown in the bar graph on the far right. From [56].

for energy confinement, intrinsic torque drive and turbulence in LOC plasmas.

The previous discussion has focussed on the explanation of energy confinement and turbulence changes across the LOC/SOC transition. Recent efforts have been directed towards an understanding of rotation reversals [65, 54, 47, 56, 57]. As was mentioned above, rotation reversals require a change in sign of the residual stress. To first order in ρ_*, contributions to the residual stress include [65]: poloidally inhomogeneous turbulence, profile shearing, radially inhomogeneous turbulence, ion orbit shifts due to radially inhomogeneous turbulence and deviations of the equilibrium distribution function from a Maxwellian. Some of these depend upon the second derivative of the kinetic profiles. A proper treatment of these mechanisms requires differing levels of complexity and sophistication in gyro-kinetic codes, incorporation of neo-classical effects, utilization of an accurate collision operator, inclusion of adiabatic electrons and a guarantee of momentum conservation [65]. The GTS code has been used to simulate rotation reversals in DIII-D plasmas [47]. Shown in Fig.29 are the calculated residual stress profiles for the SOC (top) and LOC (bottom) regimes. With SOC, there is a distinct positive peak near mid radius which gives rise to the hollow rotation profile. With LOC, the residual stress profile is near zero, consistent with the observed flat rotation profile. Also shown are the profiles of the dominant symmetry breaking mechanisms: zonal flow shearing for SOC and the turbulent intensity gradient for LOC. Similar conclusions were found for AUG rotation reversals [54].

Recent efforts have addressed the issue of cold pulse dynamics. A "non-local" response through a generic violation of local closure can occur due to meso- and macro-scale fluctuations [90]. The effects of turbulence spreading and residual stress on cold

Accepted Manuscript

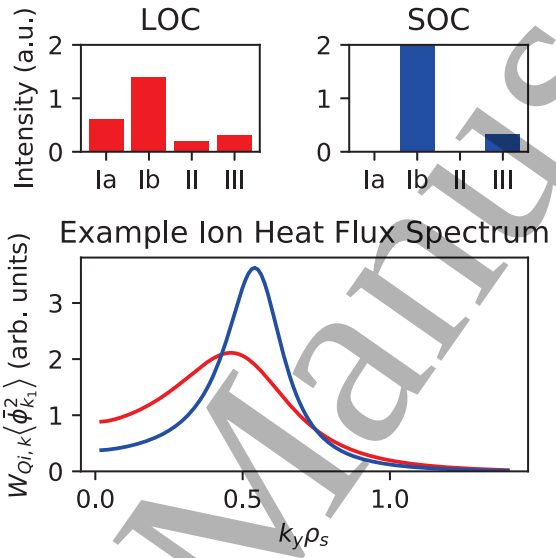

Figure 28: A qualitative illustration of the proposed LOC/SOC transition. (Top) The four mode family intensities are shown. In SOC, Families Ia and II are inactive, which necessarily shifts the balance of Family Ib. (Bottom) An example of an ion heat flux spectrum which would be consistent with the above mode families, where the SOC spectrum in blue is narrower than the LOC spectrum in red. From [56].

Accepted Manuscript

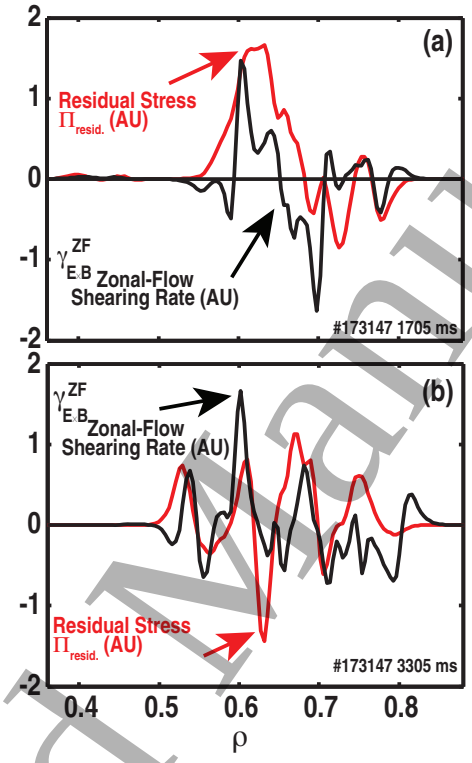

Figure 29: Radial profiles of calculated residual stress (red) and symmetry breaking mechanisms (black) for the SOC (top) and LOC (bottom) phases of a DIII-D discharge. From [47].

Accepted Manuscript

pulse response and rotation reversals have been explored [91] and the pulse polarity inversion and rotation profile reversal positions, along with dynamics, have been reproduced in the modeling. A local quasi-linear turbulent transport model has been used to simulate C-Mod cold pulse experiments, including the cut-off at high collisionality and the fast stabilization of TEMs with SOC [92]. High k simulations using TGLF-SAT1 indicate that cold pulse phenomena can be explained by the competition between density gradient driven TEM and ITG mode turbulence. Observed dynamic cold pulse behavior results from non-linear upshift of the critical gradient, profile stiffness and enhanced TEM activity.

Finally, the interplay between the residual stress and the density gradient should be considered. As was seen in the bottom frame of Fig.11, there is a maximum in density profile peaking near the LOC/SOC transition, and this effect has been seen on many devices [23, 27, 36, 37, 38, 39, 53]. The effects of TEM and ITG mode turbulence on the electron density gradient has been studied extensively on AUG [93, 94, 36, 95, 39, 53] with a maximum in the density peaking occuring at the TEM/ITG boundary, as shown in Fig.22. Shown in Fig.30 is the critical density where the density profile peaking is maximum as a function of machine major radius. These results are

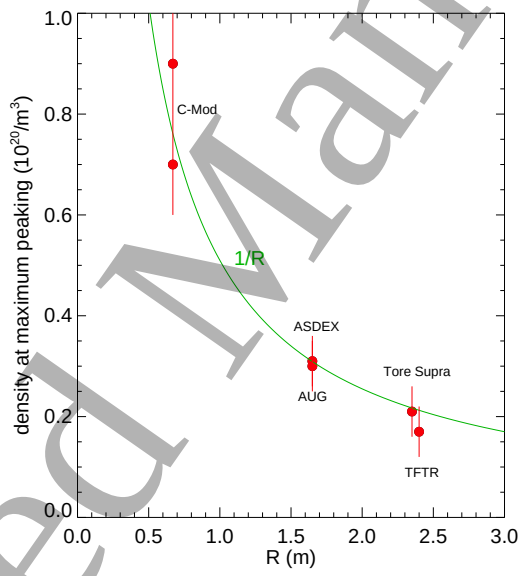

Figure 30: The critical density of the maximum electron density peaking as a function of device major radius. The 1/R curve has the same multiplier as in Fig.5 for the confinement saturation density.

consistent with a 1/R scaling, and in fact the curve in Fig.30 is exactly the same as that from the confinement saturation in Fig.5. This demonstrates yet another phenomenon connected with the LOC/SOC transition.

Accepted Manuscript

The connexion between the density and toroidal velocity gradients was first pointed out for AUG plasmas [36, 39], although the relation is not so strong for KSTAR [66]. Local linear gyro-kinetic calculations of the residual stress have been performed, imposing a finite constant tilt angle of -0.3 radians to the trapped electron mode structure [36, 39]. Shown in Fig.31a is the predicted residual stress (triangles, normalized to the momentum diffusivity) and predicted normalized toroidal rotation gradient u′ (diamonds) as a function of the measured normalized density gradient R/L$_{n_e}$. As can be

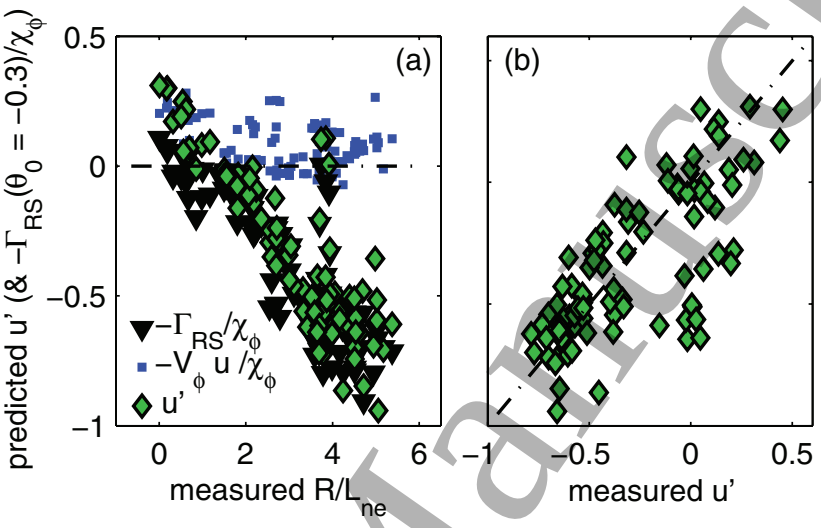

Figure 31: Local gs2 linear calculations of the contributions to u′, due to the residual stress, assuming a tilting angle of -0.3 rad (triangles) and from the Coriolis pinch (small squares) *vs.* measured R/L$_{n_e}$ (a) and the predicted values of u′ (diamonds) *vs.* measured R/L$_{n_e}$ (a) and u′ (b), in the TEM domain. From [36], used with permission.

seen there is a strong correlation between the two. Shown in Fig.31b is the predicted *versus* measured velocity gradient, again with good agreement. This analysis suggests that the observed velocity gradient can be explained by residual stresses produced by a combination of **E**×**B** and profile shearing mechanisms. The intrinsic rotation gradient may be a better parameter than the rotation magnitude at the plasma center for connecting directly with the turbulent residual stress for these reasons. Finally, it should be noted that there is no observed change in radial impurity transport across the LOC/SOC transition [38].

5. Discussion and Future Work

In this section deficiencies in the understanding of the LOC/SOC transition will be summarized and areas for future work will be outlined.

Accepted Manuscript

As was seen in Figs.2 and 15, the "neo-Alcator" scaling [19] in these cases is off by about 25%. This suggests that observations from the last 35 years should be incorporated into a new regression analysis. This exercise might reveal additional variables, besides machine dimensions, elongation and edge safety factor, which should be considered, such as Z_{eff}, background ion species and aspect ratio. In conjunction with gyro-kinetic modeling, this would help guide a quantitative theoretical understanding of the LOC regime.

Figs.1 and 2 demonstrate classic examples of SOC with a relatively flat slope. In contrast, the cases shown in Fig.3 all display a negative trend above the critical LOC/SOC density. Yet a third instance, with a positive slope in the SOC regime, is demonstrated in Fig.32 from 10 T Alcator C discharges [9, 13]. This could possibly

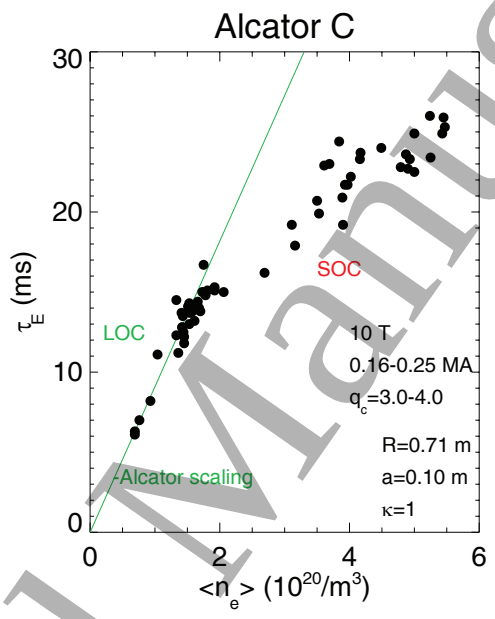

Figure 32: The global energy confinement time as a function of average density for Alcator C discharges with B_T = 10 T. From [9, 13].

be due to ITG modes not being totally unstable, either because of peaked density profiles or impurity effects as was seen in Fig.22. The SOC regime in Fig.32 actually shows a linear increase with density, but just does not go through the origin. It may be the case that the original "Alcator" scaling observations from Alcator A [3] were ironically in the SOC regime since there were no low density points shown, and the fit did not pass through the origin. All of the 6 T data points in Ref.[3] were above $1.5\times10^{20}/m^3$. Fig.14 gives $n_{crit}q_cR \sim 2.3$, and with q_c = 3.5 and R = 0.54 m yields $n_{crit} \sim 1.2\times10^{20}/m^3$, which implies that all of the points in Ref.[3] were in the SOC regime. It can similarly be argued that the FT [12] and TEXT [96] observations were also completely in the SOC regime. As for the negative slopes in Fig.3, similar results

Accepted Manuscript

Device	ν_*	$\nu_{\rm eff}$	η_i	r/a	[Ref.]
ASDEX	–	–	1.9	0.7	[23]
AUG	0.25	0.95	–	0.7	[50]
T-10	–	1.5	–	0.5	[32]
AUG	–	0.3-0.4	–	0.45	[36, 39]
C-Mod	0.4	0.3-0.4	2.0-2.6	0.7	[34, 35, 37, 77, 62, 56]
MAST	0.2-0.4	–	–	0.5-0.7	[78]
Tore Supra	–	–	1.7-2.8	0.37	[40, 87]
KSTAR	0.25	–	–	0.4-0.6	[66, 82]
DIII-D	0.5-1.0	0.4-0.7	1.8	0.6	[47]

Table 3: Rotation reversal and LOC/SOC critical collisionalities, and values for η_i from various devices, with the location r/a indicated.

occur when the energy time from magnetics measurements is used rather than the full integrated kinetic profiles of density and temperature.

As was alluded to in the discussion of Fig.5, and shown explicitly in Fig.17, the LOC/SOC transition occurs at a critical value of the product nqR, which has the same parameter dependence as the collisionality ν_*. Two different collisionalities have been considered: ν_* as defined at the end of section 2, and $\nu_{\rm eff}$, the ratio of the collision frequency to the curvature drift frequency, $\equiv \nu_{ei}/\omega_{De} \approx$ R $Z_{\rm eff}$ n_e/T_e^2, with R in m, n_e in 10^{20}/m^3 and T_e in keV [50]. The major difference between them is that ν_* is proportional to the safety factor q. Both critical values of collisionalities have been evaluated on several devices from confinement saturation, as well as rotation and turbulence propagation reversals, and examples are given in Table 3. The critical ν_* is between 0.2 and 1.0, while $\nu_{\rm eff}$ ranges from 0.3 to 1.5. From C-Mod rotation reversal data, ν_* does a slightly better job than $\nu_{\rm eff}$ matching the critical value for different plasma currents [37], perhaps because of the explicit dependence on q, either through the plasma current (as in Figs.3, 4 and 7) or the magnetic field (as in Fig.10). The q dependence could also arise through the ITG mode critical threshold which depends strongly on 1/q. At higher q, ITG modes are more easily destabilized, which leads to a lower $\nu_{\rm eff}$ for the transition. Regardless of collisionality choice, an important question arises about where across the profile the critical collisionality should be evaluated. An argument can be made for the rotation reversal anchor radius, or just inside of that, as shown in Figs.12 and 13. An area for future work is to expand Table 3 with values of ν_* and $\nu_{\rm eff}$ for all of the entries in Fig.14.

It has been argued that an increase in ion-electron coupling with increasing collisionality leads to confinement saturation [27]. This would suggest that the LOC/SOC transition occurs as the electron and ion temperatures converge with increasing collisionality, with perhaps a critical value of the T_e/T_i ratio. Shown in Fig.33a is a plot of the core electron to ion temperature ratio as a function of density for different plasma currents in 5.4 T deuterium C-Mod discharges [38]. Vertical lines indicate the critical rotation reversal densities for the three currents. The transition occurs with T_e/T_i = 1.28, 1.2 and 1.02 for 0.55, 0.8 and 1.1 MA, respectively. How close to unity the ratio

Accepted Manuscript

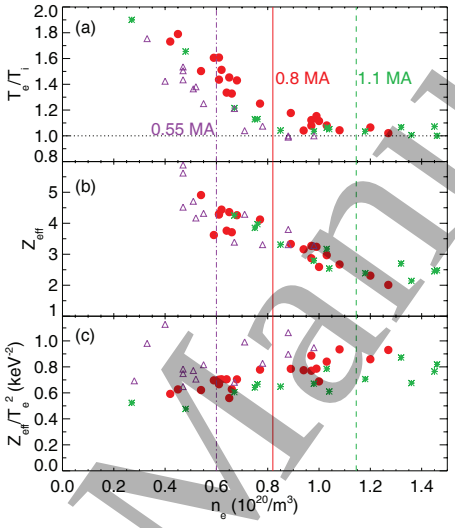

Figure 33: The central electron to ion temperature ratio (a), average $Z_{\rm eff}$ (b) and the ratio $Z_{\rm eff}/T_e{}^2$ (c) for 0.55 MA (purple triangles), 0.8 MA (red dots) and 1.1 MA (green asterisks) plasmas. Vertical lines indicate the rotation reversal density for each current: 0.55 MA (purple dash-dot), 0.8 MA (red solid) and 1.1 MA (green dashed). From [38].

Accepted Manuscript

is required for equilibration is not known, but certainly electrons and ions were totally equilibrated in C-Mod for the 1.1 MA case for densities above 1×10^{20}/m^3. For AUG plasmas, the LOC/SOC transition occured with $T_e/T_i \sim 1.5$ [39] while for Tore Supra the ratio was $\sim$1.7 [87]. These results suggest that the precise ratio of T_e/T_i, and hence electron-ion equilibration, may not be the cause of the LOC/SOC transition, but just a by product of increasing collisionality. Electron-ion equilibration brings up the T_i/T_e ratio during the LOC phase of the density ramp, which increases the ITG mode critical threshold and ensures that the ITG mode onset is delayed. At some point this cannot be delayed further, and indeed that is not expected to occur at a critical T_e/T_i, but depends upon other parameters. One should not expect a precise value for the T_e/T_i ratio since it is just one of many parameters impacting both TEM and ITG mode stability, but that does not mean that the ratio is not important. From Fig.33 the LOC/SOC transitions at a higher T_e/T_i ratio (ITG mode destabilizing) coincide with higher $Z_{\rm eff}$ (ITG mode stabilizing), suggesting that to some extent these two parameters cancel each other out. This could be an example of additional hidden parameters, on top of the nqR product, which correlate in such a fashion that their omission in a scaling does not lead to an obvious mismatch, yet are nonetheless physically important.

Several treatments [86, 42, 87, 53] have found that the effects of impurity content and ion dilution play an important role in the LOC/SOC transition. At low collisionality, high $Z_{\rm eff}$ and ion dilution stabilize ITG modes. However, even at low collisionality, carbon ITG modes are still active in the LOC regime [87], but due to their high wavenumber, they do not drive much transport. If a critical value of $Z_{\rm eff}$ or ion dilution is required for the LOC/SOC transition, it might be expected that it occurs at a fixed values of $Z_{\rm eff}$. Examination of Fig.15 in Ref.[27] reveals that the LOC/SOC transition transpires for $Z_{\rm eff}$ = 1.2, 2.0 and 2.2 for FT, ASDEX and Tore Supra, respectively. For C-Mod plasmas it occurs with $Z_{\rm eff}$ between 2.7 and 4.3, depending upon the plasma current [37, 38], as seen in Fig.33b. Comparing $Z_{\rm eff}$ at the LOC/SOC transition in FT and C-Mod, which are about the same size and magnetic field, but with markedly different values, suggests that the impurity effect is more subtle than simply the magnitude of $Z_{\rm eff}$. Furthermore, given that all tokamaks exhibit the same LOC/SOC behavior, but have different wall materials, ranging from carbon (Z=6) to molybdenum (Z=42) to tungsten (Z=74), and different levels of wall conditioning, it is hard to imagine that a common critical value of $Z_{\rm eff}$ is necessary for the transition. Ion dilution is more likely the relevant parameter, but this needs to be checked across a wide range of tokamaks. While temperature and $Z_{\rm eff}$ vary strongly with increasing density/collisionality, the ratio $Z_{\rm eff}/T_e^2$ does not, as can be seen in Fig.33c. This factor explicitly enters into both the definitions of collisionality, but does not change much for C-Mod plasmas across the LOC/SOC transition over a factor of two in plasma current.

Another factor that is important as a measure of the strength of ITG mode turbulence is η_i, the ratio of the logarithmic gradients of temperature to density. For C-Mod plasmas there is very little difference of η_i across the LOC/SOC transition, with values between 2.0 and 2.6 near the critical radius [34, 77, 62, 56], contingent upon the plasma current and magnetic field. For DIII-D, the η_i value at the transition is $\sim$1.8, depending on the radius [47]. The corresponding value for Tore Supra falls between 1.7 in the LOC regime and 2.8 with SOC [40, 87], consistent with the C-Mod and DIII-D results (see Table 3). A worthwhile exercise is to populate Table 3 with critical η_i values from

Accepted Manuscript

all devices. For kinetic electron core ITG modes, η_i is less of an organizing parameter, since density gradients are not stabilizing, but perhaps at high collisionality it is relevant, since the trapped electron drive is then effectively shut off.

Perhaps the main challenge to understanding the LOC/SOC transition is to explain why it occurs so suddenly at a critical value of the nqR product. Presumably in both the LOC and SOC regimes there is a mixture of dominant and sub-dominant TEMs and ITG modes. Why there is such a sudden change as manifested by rotation reversal and turbulence intensities is the key question which needs to be understood theoretically and captured by gyro-kinetic simulations. Another important aspect to be explained is why the critical nqR product increases with toroidal magnetic field, as was shown in Fig.14. The critical radius for rotation reversal (and temperature inversion) also needs to be understood, including the apparent connexion with the q profile. Does the location have to do with the steepest part of the temperature gradient? Another important question involves causality of the turbulence changes and rotation reversals. Does the turbulence drive the rotation or do changes in the rotation profiles drive the turbulence? Important clues are that the LOC/SOC transition occurs for $0.2 < \nu_* < 1.0$ with $\eta_i \sim 2$, and with turbulent features in the range $0.1 < k_\perp \rho_s < 0.7$.

It is important to note that rotation reversals and turbulence changes occur across the LOC/SOC transition in C-Mod plasmas with no measurable difference in the gradients of electron density, electron temperature and ion temperature [34, 62, 97, 56], or in the second derivatives [97]. These gradients are shown in Fig.34 for either side of a rotation reversal [56]. The error bars are rigorously computed using Gaussian process

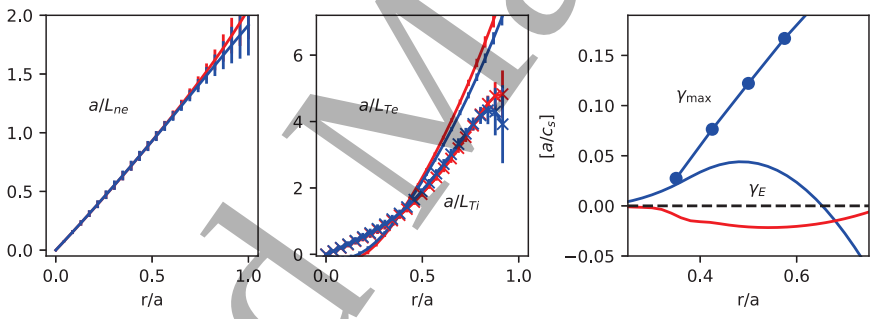

Figure 34: The normalized electron density gradients (left), normalized electron and ion temperature gradients (middle) and $\mathbf{E}\times\mathbf{B}$ shearing rates (right) for C-Mod LOC (red) and SOC (blue) plasmas. In the right panel is also shown the calculated maximum growth rate in SOC. From [56].

regression [97]. The only profile which shows a difference, and a large one at that (see Fig.12 top frame), is of the rotation. The derived $\mathbf{E}\times\mathbf{B}$ shearing rates are shown for comparison in the right panel, and exhibit a change in sign. These results challenge any model which relies on changes in density or temperature gradients (the usual instability drive terms), or in second derivatives [97].

Accepted Manuscript

Looking forward to understanding LOC/SOC phenomenology, it is crucial to consider sub-dominant modes [47, 56], as well as the interplay between TEM and ITG mode turbulence [88] in a multi-scale approach. Furthermore, for a comprehensive understanding, it would be prudent to consider electron and ion particle, momentum and heat transport channels simultaneously. From the experimental side, improved core turbulence and velocity diagnostics, with high time resolution near mid-radius, would shed light on the causality of rotation/instability changes at the LOC/SOC transition. An open area of investigation regards the effects of external heating power on LOC/SOC phenomenology, although studies have been performed on AUG, C-Mod, KSTAR and DIII-D. Finally, it is worth looking into whether the LOC/SOC transition is related to the minimum of the H-mode power threshold.

6. Acknowledgements

The authors thank the ITPA Transport and Confinement Group, and discussions with C. Angioni, C. Bourdelle, Y. Camenen, B. Duval, E. Fable, R. McDermott, D.H. Na and O. Sauter are gratefully acknowledged. Work supported at MIT by DoE Contract No. DE-FC02-99ER54512.

References

[1] Peacock N.J. *et al.*, 1969 *Nature* **224** 488.

[2] Apgar E. *et al.*, 1976 *Plasma Physics and Controlled Nuclear Fusion Research* (Proc. 6th Int. Conf. Berchtesgaden), Vol. I, p.247 (IAEA, Vienna, 1977)

[3] Gaudreau M. *et al.*, 1977 *Phys. Rev. Lett.* **39** 1266.

[4] Ascoli-Bartoli U. *et al.*, 1978 *Plasma Physics and Controlled Nuclear Fusion Research* (Proc. 7th Int. Conf. Innsbruck), Vol. I, p.149 (IAEA, Vienna, 1979)

[5] Gondhalekar A. *et al.*, 1978 *Plasma Physics and Controlled Nuclear Fusion Research* (Proc. 7th Int. Conf. Innsbruck), Vol. I, p.199 (IAEA, Vienna, 1979)

[6] Vlasenkov V.S. *et al.*, 1978 *Plasma Physics and Controlled Nuclear Fusion Research* (Proc. 7th Int. Conf. Innsbruck), Vol. I, p.211 (IAEA, Vienna, 1979)

[7] Murakami M. *et al.*, 1979 *Phys. Rev. Lett.* **42** 655.

[8] Wesley J.C. *et al.*, 1980 *Plasma Physics and Controlled Nuclear Fusion Research* (Proc. 8th Int. Conf. Brussels), Vol. I, p.35 (IAEA, Vienna, 1981)

[9] Fairfax S. *et al.*, 1980 *Plasma Physics and Controlled Nuclear Fusion Research* (Proc. 8th Int. Conf. Brussels), Vol. I, p.439 (IAEA, Vienna, 1981)

[10] Meade D. *et al.*, 1980 *Plasma Physics and Controlled Nuclear Fusion Research* (Proc. 8th Int. Conf. Brussels), Vol. I, p.665 (IAEA, Vienna, 1981)

[11] Equipe TFR, 1980 *Nucl. Fusion* **20** 1227.

Accepted Manuscript

[12] Alladio F. *et al.*, 1982 *Nucl. Fusion* **22** 479.

[13] Blackwell B. *et al.*, 1982 *Plasma Physics and Controlled Nuclear Fusion Research* (Proc. 9th Int. Conf. Baltimore), Vol. II, p.27 (IAEA, Vienna, 1983)

[14] Ejima S. *et al.*, 1982 *Nucl. Fusion* **22** 1627.

[15] Hugill J., 1983 *Nucl. Fusion* **23** 331.

[16] Efthimion P.C. *et al.*, 1984 *Phys. Rev. Lett.* **52** 1492.

[17] Greenwald M. *et al.*, 1984 *Phys. Rev. Lett.* **53** 352.

[18] Cordey J.G. *et al.*, 1984 *Plasma Physics and Controlled Nuclear Fusion Research* (Proc. 10th Int. Conf. London), Vol. I, p.167 (IAEA, Vienna, 1985)

[19] Goldston R.J., 1984 *Plasma Phys. Control. Fusion* **26** 87.

[20] Shimomura Y. *et al.*, 1987 'Empirical Scaling of Energy Confinement Time of L-Mode and Optimized Mode and Some Consideration of Reactor Core Plasma in Tokamak' JAERI Report 87-080

[21] Sengoku S. *et al.*, 1987 *J. Nucl. Mat.* **145-147** 556.

[22] Bartlett D.V. *et al.*, 1988 *Nucl. Fusion* **28** 73.

[23] Söldner F.X. *et al.*, 1988 *Phys. Rev. Lett.* **61** 1105.

[24] Brower D.L. *et al.*, 1989 *Nucl. Fusion* **29** 1247.

[25] Garbet X. *et al.*, 1992 *Nucl. Fusion* **32** 2147.

[26] Bombarda F. *et al.*, 1993 (Proc. 20th EPS Conf. on Controlled Fusion and Plasma Physics, Lisboa), Vol. I, p.115

[27] Wagner F. and Stroth U., 1993 *Plasma Phys. Control. Fusion* **35** 1321.

[28] Ryter F. *et al.*, 1994 *Plasma Phys. Control. Fusion* **36** A99.

[29] Bracco G. *et al.*, 1997 *Nucl. Fusion* **37** 759.

[30] Rettig C.L. *et al.*, 2001 *Phys. Plasmas* **8** 2232.

[31] Esipchuk Yu.V. *et al.*, 2003 *Plasma Phys. Control. Fusion* **45** 793.

[32] Kirneva N.A. *et al.*, 2008 *Plasma Phys. Control. Fusion* **50** 065004.

[33] Lin L. *et al.*, 2009 *Plasma Phys. Control. Fusion* **51** 065006.

[34] Rice J.E. *et al.*, 2011 *Nucl. Fusion* **51** 083005.

[35] Rice J.E. *et al.*, 2011 *Phys. Rev. Lett.* **107** 265001.

[36] C.Angioni *et al.*, 2011 *Phys. Rev. Lett.* **107** 215003.

Accepted Manuscript

[37] Rice J.E. *et al.*, 2012 *Phys. Plasmas* **19** 056106.

[38] Rice J.E. *et al.*, 2013 *Nucl. Fusion* **53** 033004.

[39] McDermott R.M. *et al.*, 2014 *Nucl. Fusion* **54** 043009.

[40] Arnichand H. *et al.*, 2014 *Nucl. Fusion* **54** 123017.

[41] Bernardo J. *et al.*, 2015 *Plasma Phys. Control. Fusion* **57** 035002.

[42] Ennever P. *et al.*, 2015 *Phys. Plasmas* **22** 072507.

[43] Arnichand H. *et al.*, 2015 *Nucl. Fusion* **55** 093021.

[44] Na D.H. *et al.*, 2016 *Nucl. Fusion* **56** 036011.

[45] Shi Y.J. *et al.*, 2017 *Nucl. Fusion* **57** 066040.

[46] Lebschy A. *et al.*, 2018 *Nucl. Fusion* **58** 026013.

[47] Grierson B.A. *et al.*, 2019 *Phys. Plasmas* **26** 042304.

[48] Yushmanov P.N. *et al.*, 1990 *Nucl. Fusion* **30** 1999.

[49] Greenwald M. *et al.*, 2007 *Fusion Sci. Technol.* **51** 266.

[50] Conway G.D. *et al.*, 2006 *Nucl. Fusion* **46** S799.

[51] Angioni C. *et al.*, 2003 *Phys. Plasmas* **10** 3225.

[52] Angioni C. *et al.*, 2003 *Phys. Rev. Lett.* **90** 205003.

[53] Erofeev I. *et al.*, 2017 *Nucl. Fusion* **57** 126067.

[54] Hornsby W.A. *et al.*, 2018 *Nucl. Fusion* **58** 056008.

[55] Bortolon A. *et al.*, 2006 *Phys. Rev. Lett.* **97** 235003.

[56] Cao N.M. *et al.*, 2019 *Nucl. Fusion* **59** 104001.

[57] Cao N.M. *et al.*, 2020 *Phys. Plasmas* **27** 052303.

[58] Kissick M.W. *et al.*, 1998 *Nucl. Fusion* **38** 821.

[59] Mantica P. *et al.*, 1999 *Phys. Rev. Lett.* **82** 5048.

[60] Galli P. *et al.*, 1999 *Nucl. Fusion* **39** 1355.

[61] Ryter F. *et al.*, 2000 *Nucl. Fusion* **40** 1917.

[62] Gao C. *et al.*, 2014 *Nucl. Fusion* **54** 083025.

[63] Duval B.P. *et al.*, 2007 *Plasma Phys. Control. Fusion* **49** B195.

[64] Duval B.P. *et al.*, 2008 *Phys. Plasmas* **15** 056113.

Accepted Manuscript

[65] Camenen Y. *et al.*, 2017 *Plasma Phys. Control. Fusion* **59** 034001.

[66] Na D.H. *et al.*, 2017 *Nucl. Fusion* **57** 126008.

[67] Sorbom B.N. *et al.*, 2014 *Fusion Eng. Des.* **100** 378.

[68] Mumgaard R.T. *et al.*, 2018 *60th APS-DPP Meeting, Portland, OR* GO5.00001.

[69] http://www.jt60sa.org/b/n1/introduction.htm

[70] Albanese R. *et al.*, 2017 *Nucl. Fusion* **57** 016010.

[71] Brower D.L. *et al.*, 1985 *Phys. Rev. Lett.* **54** 689.

[72] Watterson R.L. *et al.*, 1985 *Phys. Fluids* **28** 2857.

[73] Brower D.L. *et al.*, 1987 *Phys. Rev. Lett.* **59** 48.

[74] Krämer-Flecken A. *et al.*, 2004 *Nucl. Fusion* **44** 1143.

[75] Vershkov V.A. *et al.*, 2005 *Nucl. Fusion* **45** S203.

[76] Xu Y. *et al.*, 2013 *Nucl. Fusion* **53** 072001.

[77] Sung C. *et al.*, 2013 *Nucl. Fusion* **53** 083010.

[78] Hillesheim J.C. *et al.*, 2015 *Nucl. Fusion* **55** 032003.

[79] Krämer-Flecken A. *et al.*, 2015 *New J. Phys.* **17** 073007.

[80] Arnichand H. *et al.*, 2016 *Plasma Phys. Control. Fusion* **58** 014037.

[81] Trier E. *et al.*, 2017 *Nucl. Fusion* **57** 046021.

[82] Lee J.A. *et al.*, 2018 *Phys. Plasmas* **25** 022513.

[83] Diamond P.H. *et al.*, 2009 *Nucl. Fusion* **49** 045002.

[84] Ohkawa T., 1978 *Phys. Lett. A* **67** 35.

[85] Romanelli F. *et al.*, 1986 *Nucl. Fusion* **26** 1515.

[86] Porkolab M. *et al.*, 2012 *Plasma Phys. Control. Fusion* **54** 124029.

[87] Citrin J. *et al.*, 2017 *Plasma Phys. Control. Fusion* **59** 064010.

[88] Merz F. and Jenko F., 2010 *Nucl. Fusion* **50** 054005.

[89] Candy J. *et al.*, 2016 *J. Comput. Phys.* **324** 73.

[90] Ida K. *et al.*, 2015 *Nucl. Fusion* **55** 013022.

[91] Hariri F. *et al.*, 2016 *Phys. Plasmas* **23** 052512.

[92] Rodriguez-Fernandez P. *et al.*, 2018 *Phys. Rev. Lett.* **120** 075001.

Accepted Manuscript

[93] Angioni C. *et al.*, 2009 *Plasma Phys. Control. Fusion* **51** 124017.

[94] Fable E. *et al.*, 2010 *Plasma Phys. Control. Fusion* **52** 015007.

[95] Angioni C. *et al.*, 2012 *Nucl. Fusion* **52** 114003.

[96] Bravenec R.V. *et al.*, 1985 *Plasma Phys. Control. Fusion* **27** 1335.

[97] Chilenski M. *et al.*, 2017 *Nucl. Fusion* **57** 126013.

Accepted Manuscript